Multiple Intermediates in the Detergent-Induced Fusion of Lipid Vesicles

Lara G. Dresser[1], Casper Kunstmann-Olsen[1,2], Donato Conteduca[1,3], Christopher M. Hofmair[1], Nathan Smith[1], Laura Clark[1], Steven Johnson[1,4], J. Carlos Penedo[5,6], Mark C. Leake[1,4,7] & Steven D. Quinn[1,4*]

[1]School of Physics, Engineering and Technology, University of York, Heslington, York, YO10 5DD.

[2]Current Location: University of Southern Denmark, Mads Clausen Institute, Alsion 2, 6400, Sønderborg, Denmark.

[3]Current Location: Massachusetts General Hospital, 55 Fruit Street, Boston, Massachusetts, 02114, USA.

[4]York Biomedical Research Institute, University of York, Heslington, York, YO10 5DD.

[5]Centre of Biophotonics, School of Physics and Astronomy, University of St Andrews, North Haugh, St Andrews, Fife, KY16 9SS.

[6]Biomedical Sciences Research Complex, University of St Andrews, North Haugh, St Andrews, Fife, KY16 9ST.

[7]Department of Biology, University of York, Heslington, York, YO10 5DD.

*steven.quinn@york.ac.uk

Abstract

Detergent-induced vesicle interactions, critical for applications including virus inactivation, varies according to the detergent type and membrane composition, but the underlying mechanistic details remain underexplored. Here, we use a lipid mixing assay based on Förster resonance energy transfer (FRET), and single-vesicle characterization approaches to identify that sub-micron sized vesicles are induced to fuse by the non-ionic detergent Triton-X 100. We demonstrate that the process is a multi-step mechanism, characterized by discrete values of FRET efficiency between membrane-embedded fluorophores, and involves permeabilization, vesicle docking, hemi-fusion and full lipid mixing at sub-solubilizing detergent concentrations. We also dissect the kinetics of vesicle fusion to surface-tethered vesicles using a label-free quartz-crystal microbalance with dissipation monitoring approach, opening a platform for biotechnology applications. The presented strategies provide mechanistic insight into the dynamics of vesicle fusion and have implications for applications including drug delivery and sensor development where transport and manipulation of encapsulated cargo is essential.

Introduction

Detergent-membrane interactions are critical for biotechnological applications including membrane-protein extraction[1, 2], cell lysis[3], targeted drug delivery[4], and virus inactivation[5, 6]. In this context, the widely used non-ionic detergent Triton X-100 (TX-100) plays a key role by efficiently and effectively solubilizing membrane bilayers. Open questions regarding the interaction, which involves membrane fusion as a key component[7, 8, 9], include elucidating the detergent's precise molecular-level mode of action, its role in lipid-lipid interactions, and the nature and morphology of the fused species.

Thermodynamic approaches aimed at characterizing the TX-100-membrane interaction have typically used highly-controllable model-membrane systems such as supported bilayers or synthetic unilammelar vesicles (UVs) to unveil concentration requirements necessary for solubilization[10], and to disentangle the influence of membrane phase, composition, charge, and detergent: lipid ratio on the interaction[11, 12, 13]. In this context, UVs are classified as small (SUVs), large (LUVs) or giant (GUVs) reflecting vesicle sizes of < 100 nm, 100 nm - 1 μm and > 1 μm respectively. GUVs in particular have played a key role in interrogating the TX-100 membrane interaction[14] with measurements broadly confirming that TX-100 induces solubilization at concentrations above its critical micellar concentration (CMC). However, dynamic light scattering (DLS) and turbidity approaches have also revealed an intriguing growth in vesicle size under sub-solubilizing conditions[7, 8, 9, 15], pointing towards morphological changes such as membrane swelling and fusion[8] that could be harnessed for biotechnological applications.

To assess the swelling aspect, single-vesicle characterization approaches based on the fluorescence imaging of GUVs have revealed detergent-induced surface-area enhancements concurrent with the formation of dynamic pores[16, 17, 18]. Similar work also revealed that the membrane tension on both micron- and 100 nm-diameter vesicles decreases with TX-100 concentration, and the detergent introduces phase separation events in vesicles incorporating cholesterol[13, 18]. More recently, we demonstrated that variations in the efficiency of Förster resonance energy transfer (FRET) between fluorescently labelled lipids in LUVs quantitatively reports on their expansion upon TX-100 addition[19], and combinations of molecular dynamics simulations and fluorescence approaches have revealed dynamic membrane bending events and the formation of local invaginations all prior to micellization[20].

These results, and others[21], are broadly supportive of a dynamic model for TX-100 induced membrane solubilization that involves detergent saturation on the membrane surface, the formation of mixed detergent-lipid micelles, structural changes within the intact membrane, and the release of mixed micelles to solution. A more quantitative extension of this model involves the formation of phase- and composition-sensitive pores, content leakage, variations in membrane curvature and local changes to the bilayer fluidity[22]. However, the molecular mechanisms underpinning another major class of event - namely TX-100 induced vesicle fusion - are not well characterized owing in part to a lack of experimental techniques capable of capturing the entire process.

In the context of vesicle fusion, optical microscopy experiments based on the imaging of unlabelled GUVs incubated with fluorescently tagged native membranes at sub-solubilizing TX-

100 concentrations have indicated the presence of fusion by the appearance of fluorescence at the GUV site[23]. Using similar approaches, fusion between proteoliposomes and native membranes has been harnessed to enable reconstitution of transmembrane proteins into GUV bilayers after TX-100 addition[7, 8, 9, 24]. Phase contrast imaging and DLS measurements also indicate that the degree of fusion is dependent on the lipid composition, suggesting that the TX-100-membrane interaction may be a much more complex and multifaceted process. Confocal-based fluorescence experiments have also been employed to assess permeable GUV fusion, and although fusion was rarely observed, the results point towards a situation where fusion can occur due to casual contact between pores on adjacent membranes[17]. Unfortunately, conventional microscopy techniques are limited in their ability to resolve structural changes in objects smaller than 5-10 μm, can only quantify macroscopic changes in size and packing density and they lack the ability to follow molecular-level structural rearrangements on the nanoscale. There is therefore demand for alternative methods that can monitor the fusion of individual vesicles with sizes comparable to LUVs. In this regard, molecular dynamics simulations have alluded to a stock-pore mechanism of spontaneous bilayer fusion where initial vesicle docking precedes the formation of an hourglass-shaped connection between two adjoining membranes before hemi-fusion and full lipid mixing[17, 25, 26]. Whether such a mechanism occurs in detergent-rich media, and whether these states can be controllably harnessed remains an open question.

Inspired by these insights and in search of the mechanistic origins of TX-100 induced vesicle fusion, we adopted a range of ensemble- and single-vesicle characterization approaches to interrogate the structural integrity of highly curved LUVs composed of POPC (1-palmitoyl-2-oleoyl-glycero-3-phosphocholine) in response to TX-100. The LUVs used here differ from low-curvature GUV species by displaying a maximal principal curvature[27] of ~$10^7 m^{-1}$, which is an order of magnitude greater than those typically observed in GUVs. By employing particle sizing approaches including DLS and fluorescence correlation spectroscopy (FCS), we first confirm an enhancement in vesicle size under sub-solubilizing conditions. We next showcase a steady-state and time-resolved assay based on FRET[28, 29], to quantitatively assess the degree of TX-100 induced lipid mixing between vesicles. Based on the magnitude of the observed FRET efficiency between fused vesicles, coupled with morphological changes observed via electron microscopy approaches, we provide evidence that the detergent-induced fusion process is a time-dependent and multi-step process comprising vesicle docking, hemifusion and full lipid mixing prior to solubilization. While we have previously used FRET-based methods to quantitatively report on vesicle swelling[19, 30, 31], here we take advantage of enhancements in the FRET efficiency to quantify the magnitude and state of fusion. To further characterize the interaction, we also deploy a calcium-sensing assay to confirm TX-100 induces vesicle permeabilization during the process. Finally, to demonstrate the potential of TX-100 to facilitate vesicle fusion of freely-diffusing vesicles to surface-immobilized vesicles, and to extract kinetic details of the process, we deployed an acoustic-sensing approach based on quartz-crystal microbalance with dissipation monitoring (QCM-D). In this regard, the QCM-D approach offers highly sensitive real-time monitoring of surface mass and viscoelasticity, without the need for fluorescent labels. This not only opens exciting possibilities for the controllable delivery of encapsulated cargo to a substrate but may also support a range of bionanotechnological applications including diagnostic sensing, drug delivery and the formation of biomaterials.

Our discovery of a multi-step and controllable fusion process in both freely diffusing and surface-tethered vesicles at sub-solubilizing detergent concentrations provides clues to the underlying

118 TX-100-membrane interaction and may have important implications for the transport of
119 membrane proteins such as proton pumps and transport receptors[23]. We also expect the
120 presented techniques to have general applicability for assessing interactions between highly
121 curved lipid vesicles and a wide range of fusogens, such as neurotoxic proteins with important
122 biomedical significance.

123 **Results**

124 **Triton X-100 Alters the Morphology of Vesicles at Sub-Solubilizing Concentrations**

125 LUVs composed of POPC lipids were prepared by the extrusion method and confirmed to be ~200
126 nm in diameter by DLS (**Supplementary Figure 1**). We first employed FCS and DLS to assess
127 morphological changes as TX-100 was progressively added to a solution containing freely diffusing
128 vesicles. Both techniques are sensitive to the diffusion coefficient of vesicles in solution, and thus
129 quantitatively report on their hydrodynamic radius via the Stokes-Einstein relationship[32]. The FCS
130 correlation curves associated with freely diffusing LUVs labelled with 0.1 % of the fluorescent
131 membrane dye DiI progressively shifted towards longer lag times at detergent concentrations
132 below the reported CMC (~0.2-0.3 mM)[3, 33] (**Figure 1a**) - a finding that warranted further attention
133 given non-ionic surfactants typically only achieve membrane solubilization once above the CMC.
134 Here, a reduction of 40 % in vesicle diffusion coefficient, from an initial starting value of 1.28 ±
135 0.01 $\mu m^2 s^{-1}$ (±SD) in the absence of TX-100, was observed, corresponding to an increase in
136 hydrodynamic diameter (d_H) from 168 ± 1 nm to 290 ± 5 nm. In all cases, the FCS curves were best
137 fitted to a single diffusing component model (see **Methods**) with low residuals, and notably lacked
138 a significant population of micelles exhibiting higher diffusion coefficients. In line with previous
139 work[19], we attributed these observations to vesicle swelling, docking, fusion, aggregation, or
140 combinations of these effects in solution. At TX-100 concentrations beyond the CMC, the particle
141 radius reduced to ~3.5 nm which we assigned to solubilization and the formation of mixed
142 detergent-lipid micelles. DLS also confirmed a positive shift in size distribution, though we note
143 in these experiments, the lipid concentration was increased by two orders of magnitude relative
144 to the FCS work, which we hypothesised could facilitate fusion. Here, correlation curves obtained
145 from the intensity of scattered light also progressively shifted towards longer lag times (**Figure**
146 **1b**). Without detergent, the vesicles displayed a lognormal size distribution, as expected for freely
147 diffusing species, peaking at 182 nm with a low polydispersity index of 0.16 ± 0.01 (**Figure 1c,**
148 **Supplementary Figure 2**). At detergent concentrations approaching the CMC, the correlation
149 curves then revealed a 1.7-fold increase in vesicle size (**Figure 1c**) and ~4-fold increase in
150 polydispersity index (**Figure S2**), suggestive of mixed species in the ensemble. At 0.5 mM TX-100,
151 most particles displayed d_H in the range 6 – 10 nm, consistent with mixed detergent-lipid micelles.
152 However, we also observed objects with sizes ranging from 250 – 480 nm, in line with expanded,
153 fused and/or aggregated species, and to a lesser extent, particles with intermediate diameters,
154 which could be indicative of bicelles and cylindrical micelles[34] (**Figure S2**). When intensity
155 distributions were converted into volume distributions, similar trends were observed (**Figure S2**).
156 Caution should be taken in interpretating such distributions due to underlying assumptions
157 related to vesicle morphology and noise amplification, but below the CMC, the distributions
158 broadened with TX-100 addition, and a mixture of species was exposed at 0.5 mM, in line with
159 our intensity-based analysis. While a direct comparison between FCS and DLS datasets is not

entirely straightforward owing to variations in the initial lipid concentration, both analyses are broadly supportive of a progressive increase in particle size below the CMC.

Triton X-100 Induces Vesicle Fusion

To directly test for fusion, we next employed a lipid mixing assay to monitor interactions between LUVs containing 2 % DiI (FRET donor) and those containing 2 % DiD (FRET acceptor) (**Figure 2a**). Direct excitation of DiI in the absence of fusion thus yields low sensitized emission from the acceptor, however, upon vesicle fusion, lipid mixing brings the FRET pairs into close proximity, triggering enhanced sensitized acceptor emission as a consequence of non-radiative energy transfer[28, 29, 35]. A key benefit of the approach is that the total number of fluorophores remains constant throughout the fusion process, allowing for intermediate states, corresponding to different levels of lipid mixing, to be observed by quantifiable variations in the FRET efficiency (Equation 2). Ensemble FRET measurements were performed as an initial step to quantify interactions between vesicles containing DiI and DiD in response to TX-100. Here, we measured the efficiency of energy transfer using the *RatioA* parameter (Equation 3) which compares the amount of sensitized acceptor emission with that obtained by direct excitation of the acceptor. In the absence of TX-100 the intensity of sensitized acceptor emission obtained from a 1: 3 mixture of DiI: DiD vesicles was minimal, then progressively increased upon TX-100 addition towards the CMC and was anti-correlated with quenching of the donor (**Figure 2b**, **Supplementary Figure 3**). The anti-correlated nature of the DiI and DiD signals represents the classic hallmark of FRET[36], providing assurance that the observed changes are due to energy transfer. Beyond the CMC, the apparent FRET efficiency then decreased towards its initial value, reflected by an enhancement of the donor signal and corresponding reduction in sensitized acceptor emission (**Figure 2b, Supplementary Figure 3**). The increase in *RatioA* observed below the CMC indicates a progressive decrease in the mean donor-acceptor distance, supporting a model where progressive addition of TX-100 shifts the vesicle population from intact to fused species prior to solubilization and the formation of mixed micelles (**Figure 2c**). Indeed, this is reflected in the *RatioA* response, where a progressive increase towards a peak of 0.49 ± 0.03 at the CMC was observed, suggestive of morphological changes in the ensemble that results in close proximity of the dyes, followed by a reduction towards its initial value, indicative of solubilization (**Figure 2d**). To provide confidence that the observed increase in *RatioA* was due to lipid mixing, and not lipid exchange between separated vesicles, we also assessed the response of the labelled vesicles in the presence of various cyclodextrins. As previously highlighted, methyl-β-cyclodextrin (MβCD) and 2-hydropropyl-β-cyclodextrin (HPβCD) induce lipid exchange at sub-solubilizing concentrations[37], and both were added here to a solution of vesicles identical to those shown in **Figure 2b**. We observed that the sensitized acceptor emission (and corresponding *RatioA* and E_{FRET} signals) increased slightly above the baseline (E_{FRET} ~ 0.09) upon both MβCD and HPβCD addition (**Supplementary Figure 4**), and that the FRET signal was enhanced when DiI and DiD were replaced with Lipo-Cy3-CO and Lipo-Cy5-N_3 (**Supplementary Figure 4**). As previously reported, the Lipo derivatives are structurally similar to DiI and DiD (**Supplementary Figure 4**), but their FRET is enhanced upon cycloaddition[38]. We interpreted the combined data as evidence that both cyclodextrins can, to some extent, exchange DiI and DiD, however, this may not be as efficient as the exchange of unlabelled lipids. To explicitly test for DiI and DiD exchange, we also performed an experiment whereby 200 nm sized POPC vesicles labelled with 2 % DiI were separated from vesicles containing 2 % DiD by a dialysis membrane (MWCO = 3 kDa) (**Supplementary Figure 5**). In this case, we prevented DiI and DiD labelled vesicles from directly interacting, but allowed low

205 molecular weight species, including free lipids, to diffuse across the membrane (**Supplementary**
206 **Figure 5**). However, after 5 hours of dialysis in the absence and presence of TX-100, we observed
207 no evidence of DiD absorption or sensitized emission after observing the solution containing DiI.
208 We did, however, observe increased levels of scattering upon TX-100 addition, which we
209 interpreted as a signature of fusion. Taking the combined data together, the implication is that
210 the data shown in **Figure 2b** is more likely due to DiI and DiD mixing as opposed to DiI and DiD
211 exchange.

212 When additional control experiments involving the addition of TX-100 to a 1:3 mixture of LUVs
213 lacking fluorophores and those containing 2 % DiD were performed, similar results were obtained
214 (**Supplementary Figure 6**), indicating further that the observed increase in *RatioA* shown in **Figure**
215 **2b** is due to energy transfer and sensitized acceptor emission, as opposed to photophysical
216 phenomenon such as fluorescence de-quenching. We also note that the amounts of DiI and DiD
217 per vesicle and the DiI: DiD ratio were optimized (1: 3, 2 % of each dye) to maximize the magnitude
218 of the FRET response across the interaction (**Supplementary Figure 7**).

219 To confirm the presence of an energy transfer mechanism between DiI and DiD during the
220 interaction, we also evaluated the amplitude-weighted fluorescence lifetime of DiI in the absence,
221 τ_D, and presence, τ_{DA}, of DiD. In all cases, the lifetime decays displayed bi-exponential behaviour
222 after deconvolution with the instrument response function (**Supplementary Figure 8**) (Equation
223 4). As TX-100 was progressively titrated at concentrations below the CMC, τ_D progressively
224 increased from an initially self-quenched value of 0.53 ± 0.03 ns to 1.36 ± 0.02 ns, representing
225 the unquenched DiI lifetime (**Supplementary Figure 9**).We also found that τ_{DA} remained largely
226 unchanged from its initial starting value of ~0.54 ns, then sharply increased towards ~1.2 ns as
227 the concentration of TX-100 increased beyond the CMC (**Supplementary Figure 9**). We note that
228 τ_D and τ_{DA} displayed similar initial starting values which we interpreted as evidence of minimal
229 spontaneous fusion prior to injection of TX-100. The corresponding variation in the efficiency of
230 energy transfer, *E* (Equation 5), which takes into account variations in τ_{DA} relative to τ_D, then
231 displayed several common features to the *RatioA* measurements, including (i) a progressive
232 increase as the TX-100 concentration approached the CMC, (ii) a turning point at the CMC and
233 (iii) a progressive reduction towards its initial value during the solubilization step (**Figure 2e**). The
234 observed increase in *RatioA* and *E*, which effectively remove contributions from DiI de-quenching,
235 provide confidence of a TX-100-induced solubilization mechanism comprising vesicle fusion (high
236 FRET states) below the CMC, followed by solubilization and mixed micelle formation above the
237 CMC (low FRET states) (**Figure 1c**).

238 We also note the time-dependent increase in sensitized DiD emission following TX-100 injection
239 followed bi-exponential kinetics, pointing further towards a fusion process involving multiple
240 stages. In the absence of TX-100, DiD emission remained largely invariant across the observation
241 time window, also indicating a lack of spontaneous fusion, however, upon TX-100 addition, bi-
242 exponential kinetics were monitored where the amplitude weighted time constant was 273 ± 6 s
243 in the presence of 0.1 mM TX-100, and 396 ± 11 s in the presence of 0.25 mM (**Figure 2f,**
244 **Supplementary Table 1**). While the precise nature of the bi-exponential kinetics required further
245 exploration, we hypothesised that the various components are more likely to represent fusion
246 steps (for example hemi-fusion and full lipid mixing) versus combinations of lipid exchange and
247 fusion.

248 To further characterize the interaction and assess the degree of membrane permeabilization and
249 solution exchange during the TX-100 LUV interaction, we also implemented an approach based
250 on the measurement of Ca^{2+} entry into vesicles encapsulating the fluorescent calcium indicator
251 Cal-520. This approach is similar in nature to other permeabilization assays[30, 39] whereby Ca^{2+} flux
252 into intact, surface-tethered vesicles triggers a concentration dependent intensity enhancement
253 of Cal-520 at ~520 nm, as illustrated in **Supplementary Figure 10**. Prior to experimentation,
254 nonencapsulated molecules were removed by size exclusion chromatography as detailed in the
255 **Methods**. Immobilized vesicles were then imaged in buffer solution containing 10 mM Ca^{2+} with
256 and without addition of TX-100. We imaged multiple fields of view per condition, enabling
257 quantification of intensity distributions from several thousand vesicles before adding buffer
258 solution containing TX-100 and Ca^{2+}. In the absence of TX-100 and Ca^{2+}, we identified ~100
259 vesicles per 25 x 50 μm field of view, and the intensity distribution fitted to a log-normal model
260 with a peak position of 135 counts / 100 ms. When 10 mM Ca^{2+} was flushed across the same
261 vesicles, the number of fluorescent foci remained invariant, and the intensity distribution was
262 comparable, peaking at 147 counts/ 100 ms. A similar dataset was observed when the vesicles
263 were incubated with 0.025 mM TX-100 and 10 mM Ca^{2+}, however in the presence of 0.05 – 0.1
264 mM TX-100, we observed brighter foci and clearly discernible shifts in the distributions from low-
265 to-high intensities. In such cases, a 2-fold or greater increase in the probe's emission intensity
266 was observed, in line with those previously identified[30, 40]. Beyond 0.1 mM, the number of spots
267 decreased ~10-fold and each had an intensity below the baseline level, indicating Cal-520 leakage
268 from the LUVs. Control experiments performed independently on free Cal-520 in solution
269 indicated that the dye's fluorescence is insensitive to TX-100, and that it responds to Ca^{2+} in
270 detergent-rich media (**Supplementary Figure 11**), providing confidence that the observed
271 intensity enhancements are due to membrane permeabilization and Ca^{2+} transport across the
272 membrane. Importantly, the number of surface-immobilized vesicles on the surface remained
273 largely unchanged as TX-100 up to 0.1 mM was introduced. When compared with the FRET
274 measurements shown in **Figure 2d and 2e**, which indicate substantial levels of lipid mixing at
275 comparable TX-100 concentrations, the implication is that combinations of membrane
276 permeabilization and content exchange occur concurrently with fusion events in the ensemble.
277 However, whether content can be controllably recovered after release from the vesicles during
278 the permeabilization and/or solubilization stages remains an open question.

279 **The Fusion Mechanism involves Docking, Hemifusion and Full Lipid Mixing**

280 To further explore the observed structural changes, and to dissect the mechanism of fusion, we
281 next performed single-vesicle imaging via a custom-built wide-field objective-type total internal
282 reflection fluorescence microscope that enables the simultaneous imaging of DiI and DiD
283 emission[41]. Here, POPC vesicles incorporating 2 % DiI were induced to fuse with LUVs
284 incorporating 2 % DiD and 1 % biotin-PE. Fused species were then tethered to a glass coverslip
285 functionalized with biotinylated BSA and NeutrAvidin (**Figure 3a**). Vesicles were added to a
286 surface-functionalized coverslip after incubation with TX-100, and DiI and DiD fluorescence
287 trajectories were collected with 50 ms time integration. Fused vesicles were then identified by
288 the appearance of co-localized diffraction limited spots across both detection channels (**Figure**
289 **3b**) and lipid mixing between vesicles was observed via an appearance or enhancement in the
290 mean FRET efficiency per vesicle. In the absence and presence of 0 – 0.2 mM TX-100, the traces
291 obtained from > 500 individual FRET-active species were photostable over the duration of the
292 measurement (**Figure 3c, Supplementary Figure 12)** and the population distributions of FRET

293 efficiencies showed a major peak at ~0.1 (**Figure 3d**), suggestive of close contact or docking
294 between DiI and DiD-labelled vesicles, but without substantial lipid mixing. As suggested
295 elsewhere, a combination of factors, including Van der Waals, electrostatic and hydrophobic
296 interactions may be responsible for some spontaneous vesicle-vesicle interactions, even in the
297 absence of TX-100[42, 43]. As the TX-100 concentration then increased towards 0.5 mM, the traces
298 remained photostable (**Supplementary Figure 12**) and the low FRET population decreased in
299 favour of a broad distribution of high FRET states that reached a value of 0.7 at 0.5 mM, suggestive
300 of substantial lipid mixing events (**Figure 3d**). We note the observed shift in the distributions from
301 low to high FRET efficiencies broadly reflect the changes observed in the ensemble and the
302 observation of FRET states between 0.1 and 0.7 reflect the morphological heterogeneity of
303 intermediates that are structurally different from the fully fused state in which both leaflets have
304 fully mixed. We also note that as the TX-100 concentration progressively increased across the
305 titration, the total intensity per vesicle, defined as the sum of DiI and DiD emission intensities,
306 increased > 2-fold from 1325 ± 75 counts/ 50 ms at 0.1 mM TX-100 to 3070 ± 182 counts / 50 ms.
307 Since the particle size scales with the number of fluorophores[44], the data shown in **Figure 3d**
308 arises from the presence of large immobilized fusion products, as opposed to smaller mixed
309 micelles. We therefore assigned E_{FRET} = 0.7 as an indicator of full fusion, in which both leaflets of
310 the vesicle fully mixed, whereas intermediate states were assigned to hemi-fusion, where only
311 partial lipid mixing was achieved. In all cases, tri-Gaussian functions were fitted to the FRET
312 efficiency histograms, and used to identify thresholds of $E_{FRET} < 0.25$, $0.25 \geq E_{FRET} \leq 0.55$ and E_{FRET}
313 > 0.55 for classification of docked, hemi-fused and fully fused species respectively. As shown in
314 **Figure 3e**, the percentage of species exhibiting full fusion increased 5-fold across the titration,
315 whereas the number of docked species progressively diminished. While the current experiments
316 do not inform on whether TX-100 promotes vesicle docking, its insertion into intact vesicles,
317 coupled with its hydrophobicity and ability to form mixed detergent-lipid regions, could trigger
318 vesicle-vesicle interactions via a route that involves vesicle destabilization as they dynamically
319 interact[15]. Nevertheless, the imaging of single fused species via FRET provides evidence for the
320 presence of intermediate states along the fusion process, with each state characterized by
321 discrete values of FRET efficiency and thus DiI-DiD separation distance.

322 To provide further evidence for the presence of multiple intermediates, we also acquired
323 scanning electron microscopy (SEM) micrographs of vesicles in the absence and presence of
324 fusion-promoting detergent concentrations. Without TX-100, the vesicles (N = 242) were
325 predominantly spherical, exhibiting a mean circularity, ϕ, of 0.84 ± 0.15, and a mean particle size,
326 d, of 246 ± 61 nm, with little evidence of fusion (**Figure 4a, Figure 4f, Supplementary Figure 13**).
327 Upon incubation with TX-100, the mean particle size then increased 2-fold (d = 528 ± 56), the
328 majority of species were elliptical (ϕ = 0.62 ± 0.22) (**Figure 4f)** and four major species were
329 identified. First, we observed adjoined vesicles without evidence of clefting, which we interpreted
330 as early fusion products that involve vesicle docking (**Figure 4b, Supplementary Figure 14**).
331 Further examination revealed vesicles within close proximity but with a clear cleft between
332 adjacent surfaces (**Figure 4c, Supplementary Figure 15**). Based on the similarity of these
333 structures to those observed in previous studies of protein-induced vesicle fusion[45, 46], we
334 assigned these events to intermediate hemi-fusion products involving two or more vesicles.
335 Finally, we observed the appearance of much larger micron-sized ellipses (**Figure 4d,**
336 **Supplementary Figure 16**) and larger conglomerates (**Figure 4e, Supplementary Figure 17**) which
337 we interpreted as evidence of multiple fusion events. While we previously identified that TX-100
338 leads to a 20 % increase in vesicle size through swelling[19], the ellipses observed here were more

339 than double the size of a single vesicle, and are therefore more likely to represent fully fused
340 species as opposed to single expanded vesicles. Closer inspection of the surface topography of
341 such species also indicated variations in texture, protrusions, and indentations which we
342 speculate could be indicative of pore formation and/or dissociation of membrane regions (**Figure**
343 **4c**).

344 Having demonstrated TX-100 induced morphological changes by SEM, we next used Cryo-TEM to
345 visualize interactions between adjacent membranes. Here, the majority of isolated vesicles were
346 intact and unilamellar, and in line with our prior SEM measurements, they exhibited a mean
347 particle size of 249 ± 78 nm and were predominantly spherical (ϕ = 0.95 ± 0.04) (**Supplementary**
348 **Figure 18**). In agreement with previous observations[47], we also identified lower populations (< 40
349 %) of vesicles containing multiple bilayers (**Supplementary Figure 19**). Based on the prior FRET
350 and SEM analysis, and in line with models predicted for extracellular vesicle fusion[48], we
351 hypothesized that TX-100 induced fusion intermediates consist of (i) docked vesicles showing
352 close contact between the lipid bilayers, but without lipid mixing, (ii) progressive fusion of the
353 outer and inner leaflets leading to a fusion pore and (iii) development of the fused pore into a
354 fully fused state where both leaflets had fully mixed. Indeed, we identified examples of where the
355 membranes of opposing vesicles were in parallel and within close proximity (< 5 nm), but with a
356 clear barrier separating the vesicle interiors (**Figure 4g**). We also identified structures where the
357 bilayer leaflets had merged at a ~25 nm diameter contact pore, and where the two bilayers
358 transitioned continuously from one vesicle to the other (**Figure 4h**). The fully fused species, after
359 expansion of the fusion pore and upon complete content mixing, was then captured as a larger
360 fusion product containing a single bilayer, with no evidence of a barrier preventing content mixing
361 (**Figure 4i**). In some cases, we also observed examples of where further vesicles had either docked
362 to or budded from the fully fused form (**Figure 4i**). Those species classified as docked, hemifused,
363 or fully fused comprised 31 % of the population in 0.15 mM TX-100 and had a mean calliper
364 diameter of 568 ± 86 nm, which we note represents a 2.3-fold increase relative to the intact
365 vesicles (**Supplementary Figure 18**). The intermediates also displayed a shift towards lower
366 circularity values, consistent with a global morphological change from spherical intact vesicles to
367 larger, elliptical fusion products (**Supplementary Figure 18**). While the current Cryo TEM analysis
368 cannot differentiate between further docking or budding events, we note that the smaller vesicles
369 are connected to the main vesicle by a narrow aqueous channel pointing towards docked species.
370 TX-100 has, however, been shown to induce vesicle budding in GUVs of similar composition[49, 50,
371 51], and the release of smaller species cannot be ruled out. Nevertheless, these results further
372 demonstrate the heterogeneous nature of the TX-100 induced fusion products.

373 **TX-100 Facilitates Fusion between Freely-Diffusing and Surface-Immobilized Vesicles**

374 Controllable vesicle fusion to surface-tethered vesicles has vast potential for a range of
375 applications including biosensing and drug delivery[52]. We therefore explored whether TX-100
376 could controllably fuse vesicles in solution with vesicles pre-immobilized on a solid surface,
377 allowing for real-time content delivery and solution exchange. In contrast to our TIRF
378 measurements, here we assessed the kinetics of accumulated mass transfer and variations in
379 surface viscoelasticity as vesicles from solution interacted with those already pre-immobilized to
380 a substrate via QCM-D. POPC vesicles incorporating 1 % biotin-PE were first tethered to a bovine
381 serum albumin coated SiO_2 substrate incorporating 2 % biotin via NeutrAvidin as described in

382 **Figure 3a**. The frequency and dissipation signals, reflecting surface mass and viscoelasticity,
383 respectively, were then recorded under equilibrium and exposure to a constant flow rate.
384 **Supplementary Figure 20** shows representative QCM-D kinetics recorded upon injection of BSA-
385 Biotin, Neutravidin and biotinylated vesicles. After the sensors were saturated with vesicles, the
386 surface was washed with 50 mM Tris (pH 8) buffer to remove unattached species. Importantly,
387 the frequency and dissipation responses from the sensor showed little recover after the wash
388 step indicating successful surface tethering. Next, vesicles lacking biotin-PE at a final lipid
389 concentration of 0.16 mg/mL were flushed across the sensor surface in the absence and presence
390 of TX-100. Negligible vesicle deposition was noted in the absence of TX-100, indicated by the lack
391 of variation in both the frequency and dissipation responses (**Supplementary Figure 20**). When a
392 solution containing LUVs and 0.1 mM TX-100 was injected across the layer, an initial 20 Hz
393 reduction in frequency, concurrent with a 1.2-fold increase in dissipation was recorded, indicative
394 of (i) a mass gain over the period of the injection lasting tens of minutes and (ii) structural
395 rearrangements on the surface (**Figure 5a**). We assigned the bi-exponential nature of the
396 frequency decay to combinations of detergent interactions with the immobilized layer and
397 vesicle-vesicle interactions on the surface; however, the QCM-D traces are unable to clearly
398 distinguish between docked, hemi-fused and fully fused species. Experiments performed
399 independently to assess the interaction between freely diffusing TX-100 with surface-tethered
400 vesicles indicated only a 4-5 Hz shift upon injection (**Supplementary Figure 21**)[19], consistent with
401 a small mass gain on the sensor surface which we attribute to TX-100 incorporation into the
402 vesicle bilayers until saturation is reached[19]. While the QCM-D data does not report on TX-100
403 flip-flop across the bilayer, we expect this to occur rapidly, and simultaneously with its
404 incorporation[15]. Irrespective, the small shift observed here, indicates that the observed frequency
405 change shown in **Figure 5a** is mostly due to TX-100 induced vesicle-vesicle interactions on the
406 surface, as opposed to TX-100 incorporation into the surface-immobilized vesicles.

407 When the concentration of TX-100 was doubled, similar rate constants were observed (334 ± 4
408 s^{-1}) for the frequency decay though we note that the magnitude of the relative frequency and
409 dissipation responses increased 1.5- and 2.5-fold respectively pointing towards an abundance of
410 fused states on the surface (**Figure 5b**). When both surfaces were washed with solution, only a
411 partial recovery in ΔF and ΔD was observed indicating that most of the deposited material
412 irreversibly attached to the immobilized layer (**Figures 5a and 5b**). However, when detergent
413 concentrations above the CMC were in the injectant, the deposited mass returned towards the
414 initial frequency and dissipation levels during the wash step, suggesting rupture of the freely
415 diffusing vesicles upon interaction with the surface, and the subsequent removal of lipid mass
416 (**Figure 5c**). Indeed, these assertions were further confirmed when variations in frequency were
417 plotted against dissipation across the timescale of the fusion interaction (**Supplementary Figure**
418 **22**). The slope of the dissipation changes versus frequency shown in **Supplementary Figure 22**
419 reflect variations in the viscoelastic properties of the immobilized layer across time. For detergent
420 concentrations below the CMC, these changes broadly indicate that mass gain coupled with
421 viscoelasticity enhancements on the surface precede minor levels of mass loss upon washing. At
422 concentrations above the CMC, the vesicles in solution are susceptible to lysis and dissociation: a
423 finding that we note is in line with our previous ensemble FRET approaches.

424 **Discussion**

425 Several studies provide support for the hypothesis that TX-100 induces fusion of sub-micron sized
426 vesicles. For instance, optical microscopy experiments have almost exclusively demonstrated
427 GUV fusion to fluorescently-tagged native membranes at sub-solubilizing TX-100 concentrations[23]
428 and similar approaches have been employed to achieve TX-100-induced fusion between
429 proteoliposomes and native membranes, resulting in the reconstitution of transmembrane
430 proteins into GUVs[7, 8, 24]. In confocal-based fluorescence experiments, fusion was observed
431 between permeable GUVs, suggestive that the process can occur through an initial contact
432 between pores on adjoining vesicles[17]. While the mechanisms of GUV- versus LUV-detergent
433 interactions have yet to be fully worked out, previous work indicates bilayer fluctuations,
434 solubilization kinetics, detergent concentration requirements and detergent packing densities
435 depend on the vesicle size and curvature[14, 25, 30, 53]. Thus, the development of techniques to dissect
436 the multi-step mechanism of membrane fusion, especially at the higher end of the membrane
437 curvature space are required.

438 To overcome this challenge, we implemented a robust in vitro fusion assay based on the
439 measurement of energy transfer between lipophilic membrane dyes during lipid mixing. While
440 FRET-based lipid mixing assays are not without shortcomings[54] (for example, our observation that
441 DiI is initially self-quenched suggests absolute FRET values may be underestimated and caution
442 should be taken for accurate distance determinations) we demonstrate that the assay unveils
443 multiple fusion intermediates as recorded by changes in the FRET efficiency and support our
444 observations by a range of ensemble and single-particle measurements. Indeed, the cumulative
445 data strongly supports vesicle fusion over alternative processes such as lipid exchange, evident
446 by the marked increase in particle dimensions observed via DLS, SEM and Cryo-EM. Under
447 symmetric TX-100 induced lipid exchange and dynamic equilibrium, the vesicle size distribution
448 should remain relatively constant, but our experimental observations reveal significant particle
449 size variations, pointing towards a fusion mechanism as the dominant process rather than lipid
450 exchange. We do however acknowledge that we cannot completely exclude the possibility that
451 some degree of POPC lipid exchange occurs, especially as vesicles in close proximity begin to
452 interact. In this context, molecular dynamics simulations probing the interaction may be valuable.
453 Nevertheless, the specific detergent employed and the speed through which the detergent leads
454 to fusion and solubilization, categorized as “fast” or “slow” based on the detergent’s flip-flop rate
455 are highly likely to govern the underlying mechanism[15]. In instances of slow solubilization, the
456 process involves lipid extraction and/or the generation of micelles that are subsequently released
457 and exchanged with enclosed vesicles. Conversely, in the context of TX-100, the rapid flip flop
458 rate leads to the equal distribution of detergent molecules across both membrane leaflets,
459 saturation of the membrane surface, and a pathway towards solubilization that occurs via open
460 vesicular intermediates, which could facilitate fusion[25]. Here, examples of fused species induced
461 by TX-100 were visualized by SEM and Cryo-TEM, both of which provide information on the
462 morphology of the intermediates, and their occurrence under varying TX-100 conditions, and the
463 combination of experiments strongly implies that the fusion process is unidirectional, precedes
464 solubilization, and occurs via a mechanism that involves permeabilization, docking, hemifusion,
465 and full lipid mixing. This is striking for two reasons: first, the fusion process occurs at sub-
466 solubilizing detergent concentrations below the CMC and second, the fusion products observed
467 here are remarkably similar to those observed during protein-induced vesicle fusion and viral
468 fusion, raising the tantalising possibility that the observed intermediates are common, and share
469 structural similarities, regardless of the fusogen.
470

471 A direct quantitative comparison of our findings on LUVs to previous studies on both LUVs and
472 GUVs is challenging due to differences in membrane composition, vesicle size, the detergent-to-
473 lipid ratio used and the precise measurement method. Nevertheless, it is clear the fused LUVs
474 studied here, and those studied previously[13, 17, 23, 55], share common attributes. This includes
475 similar TX-100 concentration requirements to achieve fusion, observations of particle size and
476 surface area enlargements upon TX-100 addition below the CMC, and vesicle permeabilization
477 (which may suggest that TX-100 induced pores on adjacent vesicles facilitate fusion). Moreover
478 our observation of nm-sized mixed detergent-lipid micelles under solubilizing conditions is in line
479 with previous findings. Our studies on highly curved sub-micron sized vesicles are therefore
480 complementary to previous optical microscopy and light scattering measurements and open a
481 platform for exploring a matrix of environmental variables that may regulate the interaction.
482
483 Remarkably, our QCM-D results also show discrete steps of vesicle fusion and serve to highlight
484 the benefits of using TX-100 to controllably fuse vesicles to surfaces containing immobilized
485 vesicles: an important observation that may find direct relevance in a wide range of
486 biotechnological applications. For example, in targeted drug delivery, vesicles encapsulating
487 therapeutic agents are required to fuse to target sites, controllably releasing the encapsulated
488 molecule. Vesicle fusion to surfaces can also be employed to create biomimetic systems that
489 mimic natural cellular structures, or controllably modify and functionalize materials for
490 enhancement of properties including conductivity and chemical reactivity. There is also scope for
491 the fusion products to be used or manipulated in the context of sensor development, for instance
492 in the detection of specific analytes, or in microfluidic devices where vesicle fusion can be
493 employed to create well-defined membrane structures or facilitate the controllable transport and
494 manipulation of small liquid volumes. We previously suggested that TX-100, along with other non-
495 ionic surfactants induce swelling of lipid vesicles, but the absence of fusion observed with
496 detergents such as Tween-20, suggest that the fusion efficacy is detergent-dependent
497 (**Supplementary Figure 23**). Nevertheless, we expect the presented tools and techniques will be
498 used to further define the fusion mechanism when different vesicle subpopulations are
499 introduced, and to disentangle the impact of vesicle curvature, presence of lipid rafts and other
500 environmental factors (pH, ionic strength) which may regulate the interaction. Indeed, the
501 combined approaches and developed tools unambiguously dissect the underlying mechanism of
502 TX-100-induced vesicle fusion and could become an indispensable toolbox for further
503 characterizing the influence of fusogens, including those with important biomedical significance.
504 Moreover, dissecting the mechanism of LUV fusion is critical, not only for expanding our
505 fundamental knowledge of vesicle biology, but for the development of biocompatible and tissue-
506 specific delivery systems.

507 A major aspect of our results that deserves attention is that sub-solubilizing concentrations of TX-
508 100 were required to produce the fusion states described. While techniques such as isothermal
509 titration calorimetry have been applied extensively to quantify the thermodynamics of detergent
510 binding and partitioning below the CMC[12, 22, 56, 57], our work, which quantifies single vesicle
511 morphologies, implies that individual TX-100 monomers play a key role in initiating vesicle fusion.
512 This is particularly remarkable because non-ionic detergents typically achieve structural changes
513 only once above their CMCs. While further work is required to elucidate the precise role of the
514 molecule in initiating fusion, we hypothesise that sufficiently high local detergent densities on the
515 membrane may act as a nucleation site for docking, potentially via a pathway that involves
516 creation of pores. Our approaches enabled fusion intermediates to be observed up to detergent:

517 lipid ratios of ~ 5: 1, suggesting that morphological rearrangements and solution exchange are
518 initiated during LUV-detergent saturation. While membrane saturation and insertion of TX-100
519 into the bilayer may lead to local invaginations and permeabilization within intact vesicles prior
520 to fusion, it is possible that bilayer bending due to vesicle swelling could also facilitate the process.
521 It is also worth re-emphasizing a key benefit of the FRET-based strategy: unlike conventional
522 phase contrast or fluorescence-based imaging, where only a 2-dimensional plane is captured, the
523 FRET response reports on the dye separation distance across the entire 3-dimensional volume of
524 the fused species.

525 **Conclusions**

526 The approaches described here provide a general framework for dissecting the precise molecular
527 level events that lead to TX-100 induced LUV fusion in vitro. TX-100 dynamically alters the
528 conformation and integrity of both freely diffusing and surface-immobilized vesicles via a
529 mechanism involving vesicle permeabilization, docking, hemifusion, and full lipid mixing, prior to
530 solubilization and lysis. These observations provide mechanistic insights for how the widely used
531 TX-100 detergent dynamically perturbs and modulates highly curved membrane structures, even
532 at concentrations below the CMC. We anticipate that our current demonstration will be a starting
533 point for addressing many important aspects of vesicle fusion, including but not limited to, real-
534 time analysis of single-vesicle fusion events, and the influence of environmental factors, including
535 cholesterol and lipid content, and may be directly relevant to key biotechnological applications
536 where targeted vesicle fusion, especially to surfaces, is critical. We also expect that the developed
537 approaches will find general utility for unveiling the multi-step mechanism of vesicle fusion in
538 response to additional perturbative agents, including membrane-disrupting proteins and anti-
539 viral agents, and could have important implications for evaluating drug delivery efficiencies.

540 **Methods**

541 **Materials**

542 1-palmitoyl-2-oleoyl-glycero-3-phosphocholine (POPC) and 1-oleoyl-2-(12-
543 biotinyl(aminododecanoyl))-sn-glycero-3-phosphoethanolamine (biotin-PE) lipids in chloroform
544 were purchased from Avanti Polar Lipids and used without additional purification. TX-100 was
545 purchased from Sigma Aldrich and freshly suspended in 50 mM Tris buffer (pH 8) prior to each
546 use. 1,1′-Dioctadecyl-3,3,3′,3′-Tetramethylindocarbocyanine (DiI) and 1,1′-Dioctadecyl-3,3,3′,3′-
547 Tetramethylindodicarbocyanine (DiD)) were purchased from ThermoFisher Scientific and used
548 without additional purification. All lipid stock solutions were stored in chloroform at -20°C prior
549 to use, whereas DiI and DiD stock solutions from the manufacturer were stored at 4°C. Lipo-Cy3-
550 CO and Lipo-Cy5-N_3 were prepared as described elsewhere[38].

551 **Preparation of vesicles incorporating DiI and DiD**

552 Large unilamellar vesicles composed of lipid, biotin-PE and either DiI or DiD were prepared
553 immediately prior to each experiment by extrusion. Briefly, unlabelled lipids and fluorescently
554 labelled lipids were mixed in chloroform at the ratios specified in the main text prior to
555 evaporation of the solvent by application of a gentle nitrogen stream. The resulting lipid film was

556 resuspended in 50 mM Tris buffer (pH 8) and mixed well by vortex. Final solutions were then
557 extruded through a polycarbonate membrane filter with size cut off of 200 nm prior to use. The
558 same procedure was used to incorporate Lipo-Cy3-CO and Lipo-Cy5-N_3.

559 **Preparation and purification of vesicles encapsulating Cal-520 and Ca^{2+}**

560 Vesicles encapsulating either Cal-520 or Ca^{2+} were prepared as previously described[30]. Briefly,
561 chloroform was removed from POPC lipid stocks under gentle nitrogen flow, and the resulting
562 thin lipid film was dissolved and vortexed in 50 mM Tris buffer (pH 8) containing either 100 mM
563 Cal-520 or 10 mM Ca^{2+}. The solutions were then extruded at least 21 times through a 200 nm cut
564 off polycarbonate membrane filter (Avanti Polar Lipids). Vesicles were then filtered using PD-10
565 desalting columns (Sigma Aldrich) to separate non-encapsulated molecules from the loaded
566 vesicles.

567 **Fluorescence Correlation Spectroscopy**

568 FCS experiments were performed using a Zeiss LSM 880 microscope equipped with a 514 nm
569 excitation line and GaAsP detector. LUVs incorporating 99 % POPC and 0.1 % DiI were diluted in
570 50 mM Tris buffer (pH 8) to a final lipid concentration of 6 μM, pipetted onto a pre-cleaned
571 microscope slide, and sandwiched to a 1.5 glass coverslip via silica. Typical excitation powers were
572 4 μW as measured at the sample plane. Correlation curves were fitted to an equation of the form

573 $$\mathbf{G(\tau) = y_0 + \frac{1}{n}\frac{1}{(1+\tau/\tau_{diff})}\frac{1}{\sqrt{1+\tau/SP^2\tau_{diff}}}\left(1+\frac{Te^{\tau/\tau_{trip}}}{1-T}\right)}$$ (Equation 1)

574 where y_0, n, τ, $\boldsymbol{\tau}_{diff}$, SP, T and $\boldsymbol{\tau}_{trip}$ are the offset, effective number of particles in the confocal
575 volume, lag time, residence time in the confocal volume, structure parameter (which describes
576 the shape of the detection volume and is equal to $\boldsymbol{\omega_{xy}/\omega_z}$ where ω is the width of the laser spot
577 in the x, y and z directions), fraction of particles in the triplet state and residence time in triplet
578 state, respectively. Diffusion coefficients were then determined and the hydrodynamic radius was
579 estimated via the Stokes-Einstein relationship.

580 **Steady State FRET Vesicle Fusion Assay**

581 200nm sized POPC vesicles incorporating 2 % DiI were suspended in 50 mM Tris buffer (pH 8) with
582 those incorporating 2 % DiD at a DiI-LUV: DiD-LUV ratio of 1: 3 and final lipid concentration of 88
583 μM. The solution was then gently stirred by magnetic stirring at 1.5 Hz. Fluorescence emission
584 spectra were then acquired using a HORIBA Fluoromax-4 spectrophotometer with excitation
585 wavelengths of 520 nm and 620 nm. All emission spectra were corrected for background and
586 acquired under magic angle conditions. Apparent FRET efficiencies were estimated via

587 $E_{FRET} = I_A/(I_A+I_D)$ (Equation 2)

588 where I_D (λ_{ex} = 520 nm; λ_{em} = 525 – 639 nm) and I_A (λ_{ex} = 520 nm; λ_{em} = 640 – 800 nm) represent
589 the integrated fluorescence emission intensities of DiI and DiD, respectively. We also measured
590 the efficiency of energy transfer using the *RatioA* method which yields a value proportional to *E*
591 by comparing the magnitude of sensitized acceptor emission after removal of donor

592 bleedthrough to the emission obtained under direct excitation of the acceptor ($\boldsymbol{I_A^*}$) (λ_{ex} = 620 nm;
593 λ_{em} = 640 – 800 nm). Here,

594 *RatioA* = $I_A/\boldsymbol{I_A^*}$ (Equation 3)

595 Plots of *E* versus *[TX-100]* are reported as the mean and standard error from three experimental
596 runs.

597 **Time Correlated Single Photon Counting**

598 Time-resolved fluorescence decays were acquired using a FluoTime 300 instrument equipped
599 with a pulsed 530 nm excitation line (80 MHz) and PMA Hybrid 07 photomultiplier tube
600 (Picoquant). Briefly, DiI and DiD loaded POPC vesicles were mixed and magnetically stirred at 1.5
601 Hz. Fluorescence lifetime decays at an emission wavelength of 565 nm were then collected under
602 magic angle conditions until 10^4 photon counts accumulated at the decay maximum. Decay curves
603 were then fitted by iterative reconvolution of the instrument response function and the observed
604 intensity decay, I_t, using a multi-exponential decay of the form

605 $\boldsymbol{I_t} = \sum_{\boldsymbol{i=1}}^{\boldsymbol{n}} \boldsymbol{a_i e^{-\frac{t}{\tau_i}}}$ (Equation 4)

606 where a_i and t_i represent the fractional amplitudes and lifetimes of the i'th decay components.
607 FRET efficiencies, *E*, were estimated via

608 $\boldsymbol{E} = \boldsymbol{1} - \frac{\boldsymbol{\tau_{DA}}}{\boldsymbol{\tau_D}}$ (Equation 5)

609 where τ_{DA} and τ_D represent the lifetime of DiI in the presence and absence of DiD, respectively.
610 All experiments were performed in 50 mM Tris buffer (pH 8) using DiI-LUV: DiD-LUV ratios as
611 specified in the main text and final lipid concentrations of 88 μM.

612 **Dynamic Light Scattering**

613 Hydrodynamic radii of vesicles in TX-100-rich solutions were estimated using a Zetasizer mV DLS
614 system (Malvern Panalytical) equipped with a 632.8 nm laser line. Briefly, POPC LUVs at a final
615 lipid concentration of 88 μM were suspended in 50 mM Tris buffer (pH 8, n = 1.33) and TX-100
616 was added at the desired concentration. Correlation functions, g(τ), produced via the intensity of
617 scattered light were fitted to a single-species model of the form
618
619 $g(\tau) = \beta(e^{-\Gamma\tau}\left[1 + \frac{1}{2}\mu_2\tau^2\right])^{\,2}$ (Equation 6)
620
621 or a multi-species model of the form
622
623 $g(\tau) = \sum_n \left(\beta_n(e^{-\Gamma_n\tau})\right)^2$(Equation 7)
624
625 where *β* is the coherence factor, μ is the central moment of the distribution of decay rates and *Γ*
626 is the decay rate . Diffusion times, τ, were then related to the diffusion coefficients, *D*, via
627
628 $\Gamma = Dq^2$ (Equation 8)

where q is the wave factor. Hydrodynamic radii were then extracted using the Stokes-Einstein equation as discussed elsewhere[58]. All DLS measurements were performed using 178° backscattering, and intensity-size distributions were fitted to a lognormal distribution of the form

$$I = y_0 + \frac{A}{\sqrt{2\pi}wx} e^{-\frac{\left[\ln\left(\frac{x}{x_c}\right)\right]^2}{2w^2}} \quad \text{(Equation 9)}$$

where y_0 is the offset, x_c is the centre of the distribution, w is the log standard deviation and A is the area.

Single Vesicle FRET Spectroscopy

Microfluidic flow cells were constructed[41] and coated with 0.1 mg/mL BSA-Biotin, 1 mg/mL BSA and 0.2 mg/mL NeutrAvidin. Between each addition, the flow cells were washed with buffer to remove any unbound molecules. Biotinylated POPC vesicles incorporating 2 % DiD were mixed with non-biotinylated vesicles containing 2 % DiI (DiI-vesicle: DiD vesicle = 1: 3) at a final lipid concentration of 88 μM in TX-100 rich media (50 mM Tris buffer, pH 8). The fused species were then added to the functionalized coverslip for FRET-based imaging. Unbound vesicles were then removed by washing the flowcell with buffer. Objective-based TIRF microscopy was then performed on an inverted Nikon Eclipse Ti microscope containing a 100 x NA 1.49 oil immersion objective lens (Nikon)[41]. Excitation was achieved from a continuous wave 532 nm laser line (Obis, Coherent) with the diameter of the illuminated region in the field of view calculated to be 26 μm. To mitigate against photobleaching, typical excitation intensities were 8 μWcm^{-2}. DiI and DiD emission was spatially separated using a DualView Image Splitter (Photometrics) containing a dichroic (T640LPXR, Chroma) and band pass filters (ET585/65M and ET700/75M, Chroma) and imaged in parallel on a back-illuminated Prime 95b CMOS camera cooled to -30°C (Photometrics). Fluorescence and FRET trajectories from immobilized vesicles were acquired with 50 ms exposure time and recorded images were analysed in MATLAB (R2019a) using iSMS FRET microscopy software[59]. Briefly, co-localized DiI and DiD emission trajectories, termed I_D and I_A respectively, were obtained by integration of the intensity within the area containing the vesicle of interest at each time point, and apparent FRET efficiencies, E_{FRET}, were estimated as previously described. In line with previous work[28], tri-Gaussian fits were applied to the distributions shown in **Figure 3d** and based on the crossing points of the individual components, thresholds for deciding if the species were docked ($E_{FRET} < 0.25$), partially fused ($0.25 \geq E_{FRET} \leq 0.55$) or fully fused ($E_{FRET} > 0.55$) were used.

Quartz Crystal Microbalance with Dissipation Monitoring

QCM-D experiments were performed using a Q-Sense E4 system (Biolin Scientific) instrument. Briefly, SiO_2 coated substrates (Biolin Scientific) with a fundamental frequency of 5 MHz were first cleaned by UV ozone for 10 minutes, then sonicated in 2 % Hellmanex III for 10 minutes and ultrapure Milli-Q water for 20 minutes. The sensors were then dried under nitrogen before being treated with UV ozone for an additional 30 minutes. The sensors were then immersed in 4 % v/v ATES/IPA solution for 16 hours to produce an amine monolayer and dried under nitrogen before being installed in the sensor housing module. All sensors were washed with 50 mM Tris (pH 8) under a flow rate of 20 μL per minute until a stable baseline, defined as < 5 Hz shift per minute was achieved. At the start of each experiment, the sensor surfaces were functionalized

671 sequentially with 0.1 mg mL^{-1} biotinylated bovine serum albumin (BSA), 1 mg mL^{-1} BSA and 0.2
672 mg mL^{-1} NeutrAvidin as per the single-vesicle TIRF experiments. The sensors were also washed
673 with buffer after each addition to remove any unbound molecules. Vesicles incorporating 1 %
674 Biotin-PE were then flushed across the surface at a final lipid concentration of 0.25 mg mL^{-1} until
675 saturation of the surface was reached, followed by another buffer wash step. Next, POPC vesicles
676 lacking Biotin-PE at a final lipid concentration of 0.16 mg mL^{-1} were mixed with TX-100 at the
677 specified concentrations and immediately washed over the sensor surface. Unlike the TIRF
678 measurements, here we monitored the fusion of vesicles in solution to vesicles pre-tethered to
679 the sensor substrate.

680 **Scanning Electron Microscopy**

681 SEM images were acquired using a JEOL JSM 7800-F system operating at 5kV. Vesicles were
682 induced to fuse in 50 mM Tris (pH 8) conditions containing TX-100 as specified in the main text,
683 diluted, and deposited onto a silicon substrate. The solution was then evaporated, and the
684 immobilized vesicle layer was sputtered with a 5 nm layer of Pt/Pd. We note that the final
685 concentration of vesicles applied to the substrate was sub-nM to prevent the formation of
686 conglomerates that are not directly correlated to the effects of TX-100. This was confirmed by the
687 fact that for low TX-100 concentrations, and for vesicles imaged in the absence of detergent, we
688 did not observe any vesicle clusters. Vesicle diameters were determined using ImageJ, where
689 automated analysis of black and white binary images enabled separation of regions of white pixels
690 (vesicles) against a dark background. Vesicle circularity, ϕ, was measured via

691 $\phi = 4p(A/p^2)$ (Equation 10)

692 where A is the 2-dimensional surface area of the vesicle and p is the vesicle perimeter.

693 **Cryo-TEM**

694 Cryo-TEM was used to directly visualize fused vesicle species[47]. Briefly, Quantifoil copper R 1.2/1.3
695 200 mesh grids (Electron Microscopy Sciences) were prepared by glow discharging at 20 mA and
696 0.26 mbar for 1 minute in a Pelco easiGlow glow discharge system. Small volumes of vesicles pre-
697 incubated with TX-100 were than applied to the carbon side of the EM grid in 90 % humidity.
698 Excess liquid was blotted off and the grids were plunge frozen into precooled liquid ethane using
699 a Vitrobot system (Thermo Scientific), allowing fused species to be embedded and preserved
700 within a thin layer of amorphous ice. Micrographs were then obtained using a Thermo Scientific
701 Glacios Cryo-TEM microscope using an operating voltage of 200 kV and 120,000x magnification.
702 Vesicle diameters and circularities were determined using in-house computational analyses.

703 **Acknowledgements**

704 This work was supported by Alzheimer's Research UK (RF2019-A-001) and EPSRC (EP/P030017/1,
705 EP/W024063/1). We thank Prof. Daniella Barillá (Department of Biology, University of York) for
706 use of DLS instrumentation, Dr. Jamie Blaza (Department of Biology, University of York) for
707 technical expertise and use of Cryo-TEM, and Prof. Thomas Krauss (University of York) for use of
708 SEM facilities. We also thank the Bioscience Technology Facility (University of York) for use of FCS
709 and fluorescence spectroscopy facilities, and Dr Laurence Wilson (University of York) for critically
710 reading the manuscript. The authors also thank Dr. Christopher D. Spicer and Lydia J. Barber for

helpful discussions and for the generous donation of Lipo-Cy3-CO, Lipo-Cy5-N_3 and dialysis kits. We also thank the peer reviewers for critically evaluating our manuscript and for providing positive and constructive comments.

Data Availability

The datasets generated during the current study are available from the corresponding author on reasonable request.

Author Contributions

S. D. Q. designed the research and wrote the manuscript with the help of all other co-authors. L. G. D., C. K., D. C., C. M. H., N. S, and S. D. Q. collected the data and performed the research. L. G. D., C. K., D. C., C. M. H., N. S., L. C., J. C. P., M. C. L., and S. D. Q. analyzed the data. S. D. Q. was the project administrator.

Competing Interests

The authors declare no competing interests.

References

1. Gennuso F, Fernetti C, Tirolo C, Testa N, L'Episcopo F, Caniglia S*, et al.* Bilirubin protects astrocytes from its own toxicity by inducing up-regulation and translocation of multidrug resistance-associated protein 1 (Mrp1). *Proc Natl Acad Sci U S A* 2004, **101**(8)**:** 2470-2475.

2. Rajagopal A, Pant AC, Simon SM, Chen Y. In vivo analysis of human multidrug resistance protein 1 (MRP1) activity using transient expression of fluorescently tagged MRP1. *Cancer Res* 2002, **62**(2)**:** 391-396.

3. Koley D, Bard AJ. Triton X-100 concentration effects on membrane permeability of a single HeLa cell by scanning electrochemical microscopy (SECM). *Proc Natl Acad Sci U S A* 2010, **107**(39)**:** 16783-16787.

4. Ishkhanyan H, Rhys NH, Barlow DJ, Lawrence MJ, Lorenz CD. Impact of drug aggregation on the structural and dynamic properties of Triton X-100 micelles. *Nanoscale* 2022, **14**(14)**:** 5392-5403.

5. Welch SR, Davies KA, Buczkowski H, Hettiarachchi N, Green N, Arnold U*, et al.* Analysis of Inactivation of SARS-CoV-2 by Specimen Transport Media, Nucleic Acid Extraction Reagents, Detergents, and Fixatives. *J Clin Microbiol* 2020, **58**(11).

6. Colavita F, Quartu S, Lalle E, Bordi L, Lapa D, Meschi S*, et al.* Evaluation of the inactivation effect of Triton X-100 on Ebola virus infectivity. *J Clin Virol* 2017, **86:** 27-30.

7. Kragh-Hansen U, le Maire M, Moller JV. The mechanism of detergent solubilization of liposomes and protein-containing membranes. *Biophys J* 1998, **75**(6)**:** 2932-2946.

8. Urbaneja MA, Goni FM, Alonso A. Structural changes induced by Triton X-100 on sonicated phosphatidylcholine liposomes. *Eur J Biochem* 1988, **173**(3)**:** 585-588.

9. Paternostre MT, Roux M, Rigaud JL. Mechanisms of membrane protein insertion into liposomes during reconstitution procedures involving the use of detergents. 1. Solubilization of large unilamellar liposomes (prepared by reverse-phase evaporation) by triton X-100, octyl glucoside, and sodium cholate. *Biochemistry* 1988, **27**(8)**:** 2668-2677.

10. Lete MG, Monasterio BG, Collado MI, Medina M, Sot J, Alonso A*, et al.* Fast and slow biomembrane solubilizing detergents: Insights into their mechanism of action. *Colloid Surface B* 2019, **183**.

11. Clark ST, Arras MML, Sarles SA, Frymier PD. Lipid shape determination of detergent solubilization in mixed-lipid liposomes. *Colloids Surf B Biointerfaces* 2020, **187:** 110609.

12. Heerklotz H, Seelig J. Titration calorimetry of surfactant-membrane partitioning and membrane solubilization. *Biochim Biophys Acta* 2000, **1508**(1-2)**:** 69-85.

13. Mattei B, Franca AD, Riske KA. Solubilization of binary lipid mixtures by the detergent Triton X-100: the role of cholesterol. *Langmuir* 2015, **31**(1)**:** 378-386.

14. Seddon AM, Curnow P, Booth PJ. Membrane proteins, lipids and detergents: not just a soap opera. *Biochim Biophys Acta* 2004, **1666**(1-2)**:** 105-117.

15. Lichtenberg D, Ahyayauch H, Goni FM. The mechanism of detergent solubilization of lipid bilayers. *Biophys J* 2013, **105**(2)**:** 289-299.

16. Sudbrack TP, Archilha NL, Itri R, Riske KA. Observing the solubilization of lipid bilayers by detergents with optical microscopy of GUVs. *J Phys Chem B* 2011, **115**(2)**:** 269-277.

17. Mattei B, Lira RB, Perez KR, Riske KA. Membrane permeabilization induced by Triton X-100: The role of membrane phase state and edge tension. *Chem Phys Lipids* 2017, **202:** 28-37.

18. Casadei BR, Domingues CC, de Paula E, Riske KA. Direct visualization of the action of Triton X-100 on giant vesicles of erythrocyte membrane lipids. *Biophys J* 2014, **106**(11)**:** 2417-2425.

19. Dalgarno PA, Juan-Colas J, Hedley GJ, Pineiro L, Novo M, Perez-Gonzalez C*, et al.* Unveiling the multi-step solubilization mechanism of sub-micron size vesicles by detergents. *Sci Rep* 2019, **9**(1)**:** 12897.

20. Drab M, Pandur Z, Penic S, Iglic A, Kralj-Iglic V, Stopar D. A Monte Carlo study of giant vesicle morphologies in nonequilibrium environments. *Biophys J* 2021, **120**(20)**:** 4418-4428.

21. Aleksanyan M, Faizi HA, Kirmpaki MA, Vlahovska PM, Riske KA, Dimova R. Assessing membrane material properties from the response of giant unilamellar vesicles to electric fields. *Adv Phys X* 2023, **8**(1).

22. Arnulphi C, Sot J, Garcia-Pacios M, Arrondo JLR, Alonso A, Goni FM. Triton X-100 partitioning into sphingomyelin Bilayers at subsolubilizing detergent concentrations: Effect of lipid phase and a comparison with Dipalmitoylphosphatidylcholine. *Biophysical Journal* 2007, **93**(10)**:** 3504-3514.

23. Dezi M, Di Cicco A, Bassereau P, Levy D. Detergent-mediated incorporation of transmembrane proteins in giant unilamellar vesicles with controlled physiological contents. *Proc Natl Acad Sci U S A* 2013, **110**(18)**:** 7276-7281.

24. Skrzypek R, Iqbal S, Callaghan R. Methods of reconstitution to investigate membrane protein function. *Methods* 2018, **147:** 126-141.

25. Pizzirusso A, De Nicola A, Sevink GJA, Correa A, Cascella M, Kawakatsu T*, et al.* Biomembrane solubilization mechanism by Triton X-100: a computational study of the three stage model. *Phys Chem Chem Phys* 2017, **19**(44)**:** 29780-29794.

26. Marrink SJ, Mark AE. The mechanism of vesicle fusion as revealed by molecular dynamics simulations. *J Am Chem Soc* 2003, **125**(37)**:** 11144-11145.

27. Schamberger B, Ziege R, Anselme K, Ben Amar M, Bykowski M, Castro APG*, et al.* Curvature in Biological Systems: Its Quantification, Emergence, and Implications across the Scales. *Adv Mater* 2023, **35**(13)**:** e2206110.

28. Yoon TY, Okumus B, Zhang F, Shin YK, Ha T. Multiple intermediates in SNARE-induced membrane fusion. *Proc Natl Acad Sci U S A* 2006, **103**(52)**:** 19731-19736.

29. Diao J, Ishitsuka Y, Lee H, Joo C, Su Z, Syed S*, et al.* A single vesicle-vesicle fusion assay for in vitro studies of SNAREs and accessory proteins. *Nat Protoc* 2012, **7**(5)**:** 921-934.

30. Dresser L, Graham SP, Miller LM, Schaefer C, Conteduca D, Johnson S*, et al.* Tween-20 Induces the Structural Remodeling of Single Lipid Vesicles. *J Phys Chem Lett* 2022, **13**(23)**:** 5341-5350.

31. Juan-Colas J, Dresser L, Morris K, Lagadou H, Ward RH, Burns A*, et al.* The Mechanism of Vesicle Solubilization by the Detergent Sodium Dodecyl Sulfate. *Langmuir* 2020, **36**(39)**:** 11499-11507.

32. Elsayed MMA, Ibrahim MM, Cevc G. The effect of membrane softeners on rigidity of lipid vesicle bilayers: Derivation from vesicle size changes. *Chem Phys Lipids* 2018, **210:** 98-108.

849 33. Zhang L, Chai X, Sun P, Yuan B, Jiang B, Zhang X*, et al.* The Study of the Aggregated
850 Pattern of TX100 Micelle by Using Solvent Paramagnetic Relaxation Enhancements.
851 *Molecules* 2019, **24**(9).
852
853 34. Mkam Tsengam IK, Omarova M, Kelley EG, McCormick A, Bothun GD, Raghavan SR*,*
854 *et al.* Transformation of Lipid Vesicles into Micelles by Adding Nonionic
855 Surfactants: Elucidating the Structural Pathway and the Intermediate Structures. *J*
856 *Phys Chem B* 2022, **126**(11)**:** 2208-2216.
857
858 35. Francois-Martin C, Pincet F. Actual fusion efficiency in the lipid mixing assay -
859 Comparison between nanodiscs and liposomes. *Sci Rep-Uk* 2017, **7**.
860
861 36. Roy R, Hohng S, Ha T. A practical guide to single-molecule FRET. *Nat Methods* 2008,
862 **5**(6)**:** 507-516.
863
864 37. Huang Z, London E. Effect of cyclodextrin and membrane lipid structure upon
865 cyclodextrin-lipid interaction. *Langmuir* 2013, **29**(47)**:** 14631-14638.
866
867 38. Jumeaux C, Spicer CD, Charchar P, Howes PD, Holme MN, Ma L*, et al.* Strain-
868 Promoted Cycloadditions in Lipid Bilayers Triggered by Liposome Fusion. *Angew*
869 *Chem Int Ed Engl* 2024, **63**(14)**:** e202314786.
870
871 39. De S, Wirthensohn DC, Flagmeier P, Hughes C, Aprile FA, Ruggeri FS*, et al.* Different
872 soluble aggregates of Aβ42 can give rise to cellular toxicity through different
873 mechanisms. *Nat Commun* 2019, **10**.
874
875 40. Flagmeier P, De S, Wirthensohn DC, Lee SF, Vincke C, Muyldermans S*, et al.*
876 Ultrasensitive Measurement of Ca2+ Influx into Lipid Vesicles Induced by Protein
877 Aggregates. *Angew Chem Int Edit* 2017, **56**(27)**:** 7750-7754.
878
879 41. Dresser L, Hunter P, Yendybayeva F, Hargreaves AL, Howard JAL, Evans GJO*, et al.*
880 Amyloid-beta oligomerization monitored by single-molecule stepwise
881 photobleaching. *Methods* 2021, **193:** 80-95.
882
883 42. Kyoung M, Sheets ED. Vesicle diffusion close to a membrane: intermembrane
884 interactions measured with fluorescence correlation spectroscopy. *Biophys J* 2008,
885 **95**(12)**:** 5789-5797.
886
887 43. Shoemaker SD, Vanderlick TK. Intramembrane electrostatic interactions
888 destabilize lipid vesicles. *Biophys J* 2002, **83**(4)**:** 2007-2014.
889
890 44. Andronico LA, Jiang Y, Jung SR, Fujimoto BS, Vojtech L, Chiu DT. Sizing Extracellular
891 Vesicles Using Membrane Dyes and a Single Molecule-Sensitive Flow Analyzer. *Anal*
892 *Chem* 2021, **93**(14)**:** 5897-5905.
893
894 45. Chlanda P, Mekhedov E, Waters H, Schwartz CL, Fischer ER, Ryham RJ*, et al.* The
895 hemifusion structure induced by influenza virus haemagglutinin is determined by
896 physical properties of the target membranes. *Nat Microbiol* 2016, **1**(6).
897

46. Ward AE, Kiessling V, Pornillos O, White JM, Ganser-Pornillos BK, Tamm LK. HIV-cell membrane fusion intermediates are restricted by Serincs as revealed by cryo-electron and TIRF microscopy. *J Biol Chem* 2020, **295**(45)**:** 15183-15195.

47. Quinn SD, Dresser L, Graham S, Conteduca D, Shepherd J, Leake MC. Crowding-induced morphological changes in synthetic lipid vesicles determined using smFRET. *Front Bioeng Biotechnol* 2022, **10:** 958026.

48. Morandi MI, Busko P, Ozer-Partuk E, Khan S, Zarfati G, Elbaz-Alon Y*, et al.* Extracellular vesicle fusion visualized by cryo-electron microscopy. *PNAS Nexus* 2022, **1**(4)**:** pgac156.

49. Nomura F, Nagata M, Inaba T, Hiramatsu H, Hotani H, Takiguchi K. Capabilities of liposomes for topological transformation. *Proc Natl Acad Sci U S A* 2001, **98**(5)**:** 2340-2345.

50. Staneva G, Seigneuret M, Koumanov K, Trugnan G, Angelova MI. Detergents induce raft-like domains budding and fission from giant unilamellar heterogeneous vesicles: a direct microscopy observation. *Chem Phys Lipids* 2005, **136**(1)**:** 55-66.

51. Tomita T, Sugawara T, Wakamoto Y. Multitude of morphological dynamics of giant multilamellar vesicles in regulated nonequilibrium environments. *Langmuir* 2011, **27**(16)**:** 10106-10112.

52. Abraham S, Heckenthaler T, Bandyopadhyay D, Morgenstern Y, Kaufman Y. Quantitative Description of the Vesicle Fusion Mechanism on Solid Surfaces and the Role of Cholesterol. *J Phys Chem C* 2018, **122**(40)**:** 22985-22995.

53. Elsayed MM, Cevc G. The vesicle-to-micelle transformation of phospholipid-cholate mixed aggregates: a state of the art analysis including membrane curvature effects. *Biochim Biophys Acta* 2011, **1808**(1)**:** 140-153.

54. Gnopo YMD, Putnam D. A lipid mixing assay to accurately quantify the fusion of outer membrane vesicles. *Methods* 2020, **177:** 74-79.

55. Niroomand H, Venkatesan GA, Sarles SA, Mukherjee D, Khomami B. Lipid-Detergent Phase Transitions During Detergent-Mediated Liposome Solubilization. *J Membr Biol* 2016, **249**(4)**:** 523-538.

56. Ollila F, Slotte JP. Partitioning of Triton X-100, deoxycholate and C
EO
into bilayers composed of native and hydrogenated egg yolk sphingomyelin. *Bba-Biomembranes* 2002, **1564**(1)**:** 281-288.

57. Caritá AC, Cavalcanti RRM, Oliveira MSS, Riske KA. Solubilization of biomimetic lipid mixtures by some commonly used non-ionic detergents. *Chemistry and Physics of Lipids* 2023, **255**.

58. Stetefeld J, McKenna SA, Patel TR. Dynamic light scattering: a practical guide and applications in biomedical sciences. *Biophys Rev* 2016, **8**(4)**:** 409-427.

59. Preus S, Noer SL, Hildebrandt LL, Gudnason D, Birkedal V. iSMS: single-molecule FRET microscopy software. *Nat Methods* 2015, **12**(7)**:** 593-594.

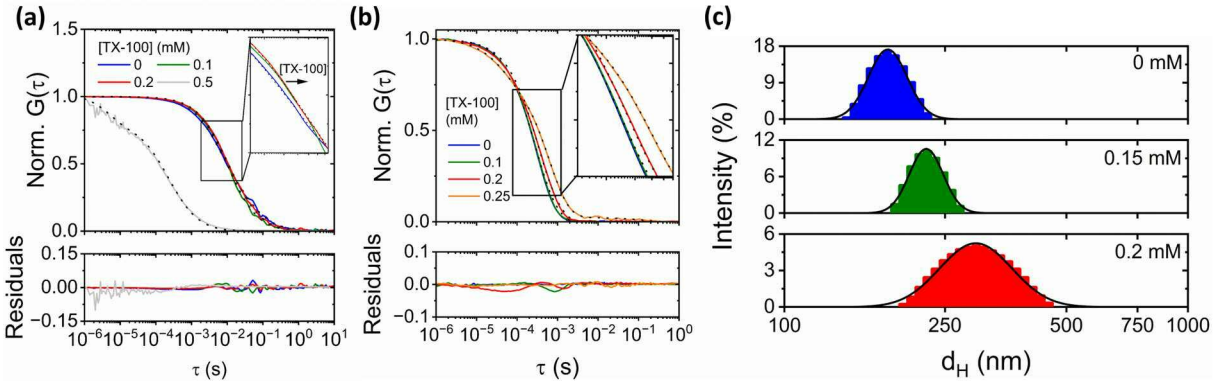

Figure 1. Characterization of vesicle-detergent interactions at sub-solubilizing TX-100 concentrations. (a) Top: Normalized variation in FCS correlation curves (solid lines) and fits (dotted lines) associated with interactions between LUVs and 0 (blue), 0.1 (green), 0.2 (red) and 0.5 (grey) mM TX-100 at 21°C. Bottom: corresponding residuals of the fits. (b) Top: Normalized variation in DLS correlation curves (solid lines) and fits (dotted lines) associated with interactions between LUVs and 0 (blue), 0.1 (green), 0.2 (red) and 0.25 (orange) mM TX-100 at 21°C. Bottom: residuals of the fits. (c) Corresponding hydrodynamic diameter distributions obtained from LUVs in the absence (blue) and presence of 0.15 (green) and 0.2 (red) mM TX-100. The solid black lines represent lognormal fits with peak d_H values of 182.6 ± 0.1 nm (Chi-squared χ_r^2 = 0.02) (top), 226.8 ± 0.2 nm (χ_r^2 = 0.02) (middle) and 311.2 ± 0.7 nm (χ_r^2 = 0.01) (bottom), respectively.

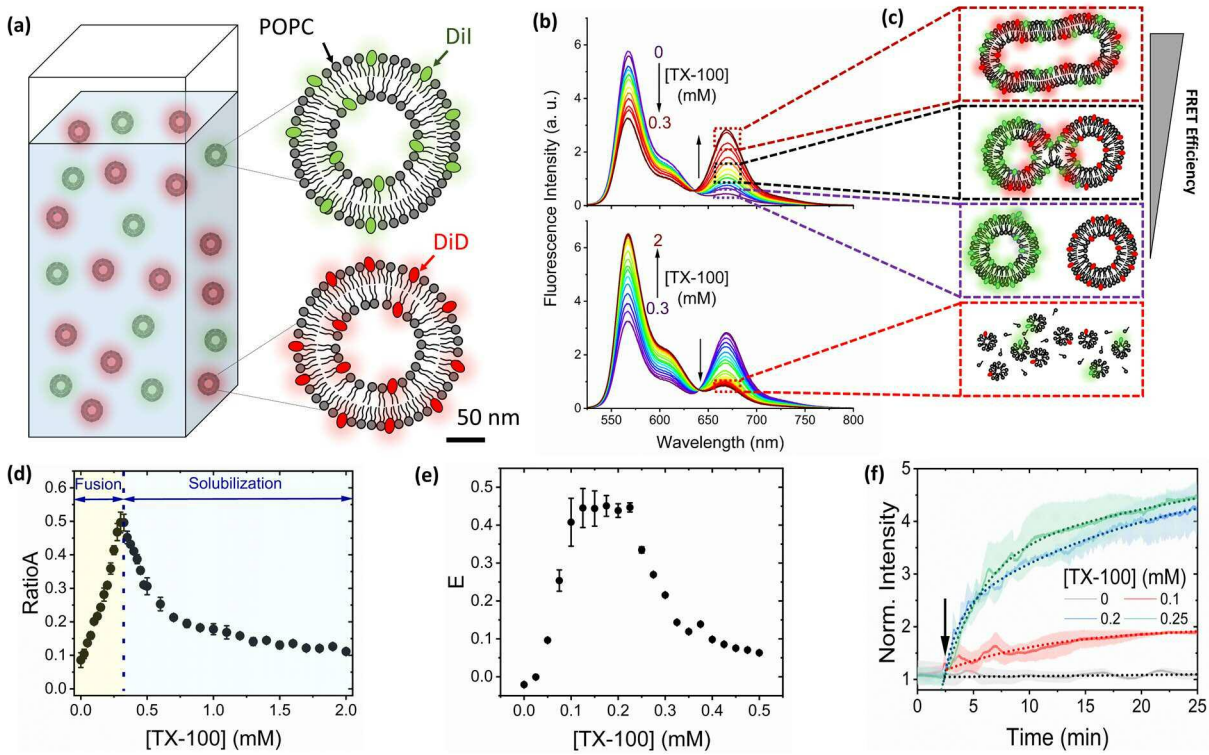

Figure 2. TX-100 induces vesicle fusion. (a) Schematic illustration of the lipid mixing assay. POPC LUVs containing 2 % DiI (green) and 2 % DiD (red) are incubated at a 1: 3 ratio. (b) Representative variation in fluorescence emission spectra (λ_{ex} = 520 nm) obtained from LUVs in the presence of 0 – 0.3 mM (top panel) and 0.3 mM – 2 mM TX-100 (bottom panel) at 21ºC. (c) Mixing LUVs with TX-100 results in FRET enhancements assigned to vesicle docking and fusion prior to FRET reductions attributed to micellization. (d) Corresponding variation in *RatioA*. (e) Variation in FRET efficiency, *E*, as estimated from changes in τ_D and τ_{DA} across the titration. Data points represent the mean and standard error of the mean from three separated experimental runs. (f) Time-dependent variation in DiD emission upon injection of TX-100 at 21ºC (λ_{ex} = 520 nm). The grey dashed line corresponds to a linear fit, coloured dashed lines correspond to bi-exponential fits and the shaded areas correspond to the SE. The arrow indicates the point of TX-100 injection.

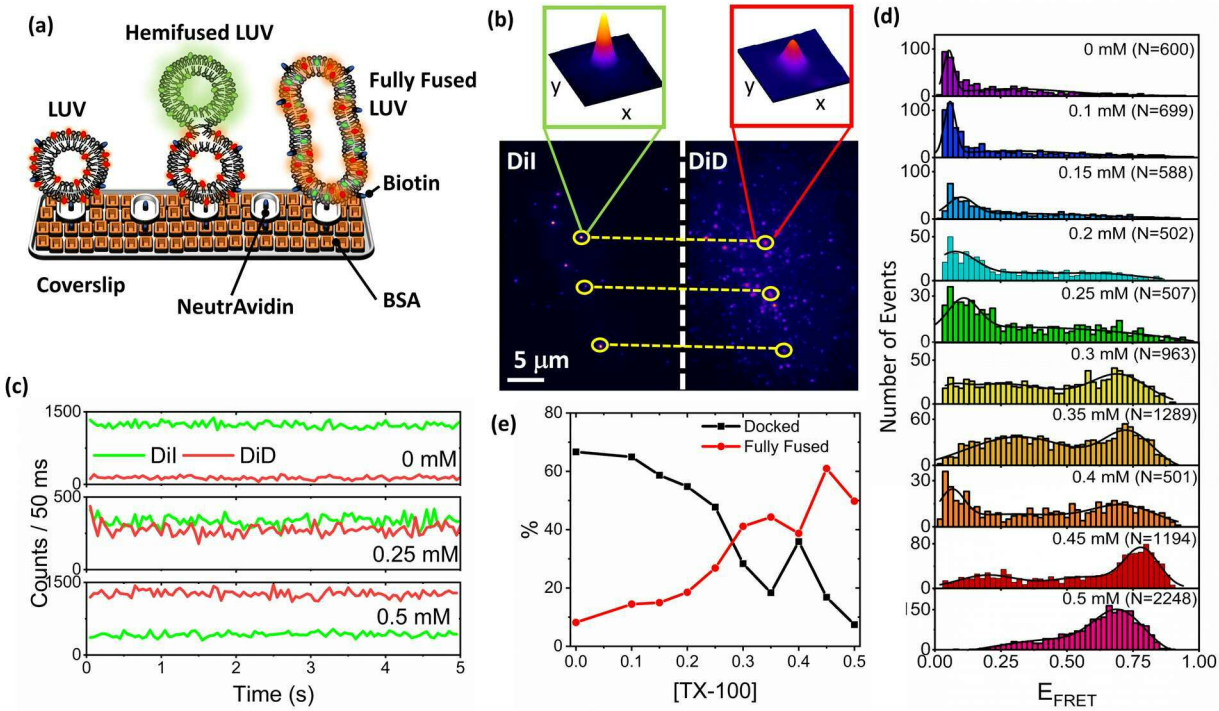

Figure 3. TX-100 induces vesicle docking, hemifusion and full lipid mixing. (a) Schematic illustration of the immobilization scheme. LUVs incorporating 2 % DiD and 1 % Biotin-PE were fused with LUVs incorporating 2 % DiI at 21°C and attached to a coverslip via BSA, biotin and NeutrAvidin. (b) Representative TIRF image obtained from surface-tethered LUVs in the presence of TX-100, showing co-localized DiI and DiD regions (yellow circles) (λ_{ex} = 532 nm). Insets: 3D intensity profiles of DiI and DiD emission obtained from a single fusion product. (c) Representative DiI (green) and DiD (red) intensity traces obtained from individually fused LUVs in the absence and presence of TX-100. (d) Histograms of the mean apparent FRET efficiency obtained from N > 500 surface immobilized vesicles before and after incubation with TX-100 rich solutions. Solid black lines represent tri-Gaussian fits. (e) Variation in the number of docked (E_{FRET} < 0.25) versus fully fused (E_{FRET} > 0.55) species observed as a function of TX-100.

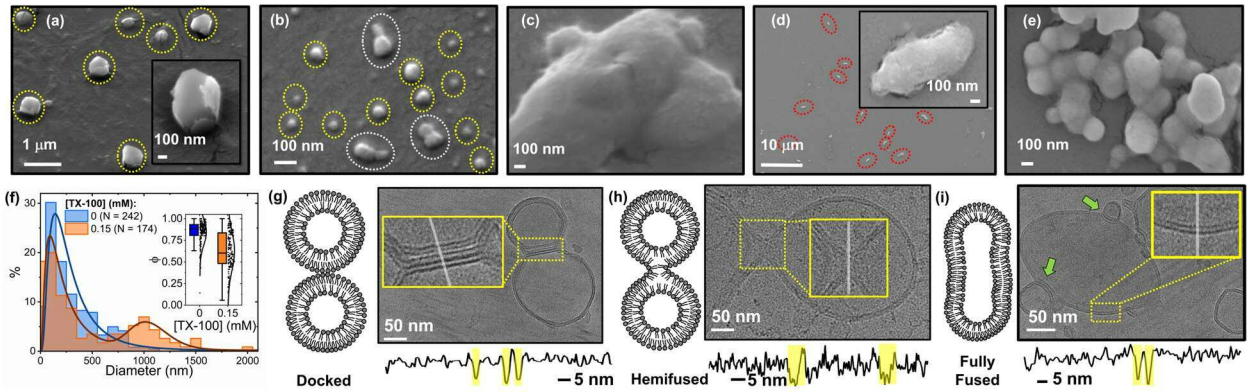

Figure 4. Confirmation of fused vesicles by SEM and Cryo-TEM. (a) SEM micrographs of intact vesicles in the absence and (b-e) presence of 0.15 mM TX-100 showing intact immobilized vesicles (yellow dashed regions), docked vesicles (white dashed regions), and large elliptical species (red dashed regions) assigned to full fusion. Vesicles were prepared and incubated with TX-100 at 21°C. (f) Size distribution histograms obtained from vesicles in the absence (blue) and presence (orange) of 0.15 mM TX-100. Inset: comparative box plots summarizing the corresponding variation in particle circularity. The boxes represent the interquartile ranges, the upper and lower whiskers represent the 5th and 95th percentiles, and the solid lines inside the boxes represent the medians. (g) Schematic (left panel) and representative cryo-TEM image (right panel) of docked, (h) hemi-fused and (i) fully fused species. Insets: regions of interest at higher magnification showing bilayers defined by the luminal grey level distribution (bottom panels). The green arrows indicate further docking or budding events.

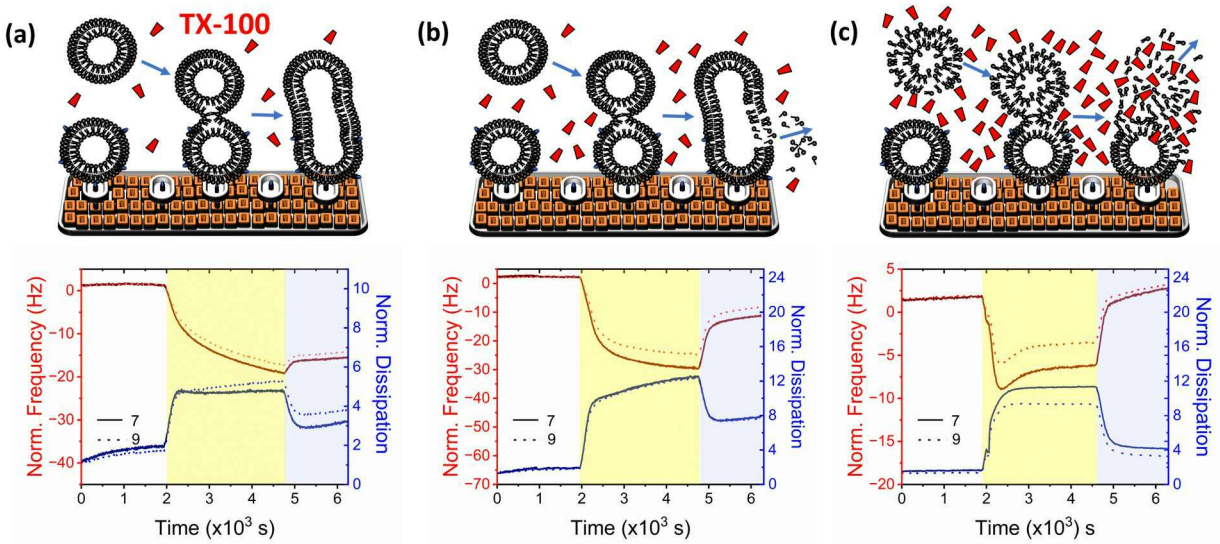

Figure 5. QCM-D analysis of TX-100 induced vesicle fusion on solid surfaces. Schematic illustrations (top panels) and normalized variation in frequency (red) and dissipation (blue) (bottom panels) associated with the 7th (solid lines) and 9th (dashed lines) harmonics upon injection of LUVs and (a) 0.1 mM, (b) 0.2 mM and (c) 0.3 mM TX-100 to a surface functionalized with BSA-biotin, NeutrAvidin and biotinylated LUVs. As illustrated, TX-100 induces a time-dependent increase in mass on the surface due to vesicles in solution merging with anchored vesicles, and minimal material is removed during surface washing when the TX-100 concentration is below the CMC. In contrast, tethered species lyse and dissociate when the detergent concentration exceeds the CMC. Injection of TX-100 and freely diffusing LUVs is denoted by the yellow shaded areas and was performed after washing the vesicle saturated surface with 50 mM Tris buffer (pH 8). The blue shaded areas correspond to the final wash step when post-interaction, the surface was rinsed with buffer. All experiments were performed at 21°C.